Atmospheric Environment 320 (2024) 120336

Contents lists available at ScienceDirect

Atmospheric Environment

journal homepage: www.elsevier.com/locate/atmosenv

# Investigating the Presence of Biomass Burning Events at Ny-Ålesund: Optical and Chemical Insights from Summer-Fall 2019

Simone Pulimeno [a,b,*], Federica Bruschi [c], Matteo Feltracco [a], Mauro Mazzola [b], Stefania Gilardoni [b], Stefano Crocchianti [c], David Cappelletti [c,b], Andrea Gambaro [a], Elena Barbaro [d]

[a] Ca' Foscari University of Venice, Department of Environmental Sciences, Informatics and Statistics, Via Torino 155, Venice, 30172, Italy
[b] National Research Council, Institute of Polar Sciences (CNR-ISP), Via Gobetti 101, Bologna, 40129, Italy
[c] University of Perugia, Department of Chemistry, Biology and Biotechnologies, Via dell'Elce di Sotto 8, Perugia, 06123, Italy
[d] National Research Council, Institute of Polar Sciences (CNR-ISP), Via Torino, 155, Venice, 30172, Italy

## HIGHLIGHTS

- 12 mild pollution events have been identified investigating optical properties.
- Biomass burning's contribution accounted for 2% of the total concentration.
- Most of the events were detected during the fall.
- The latest events in December may have been impacted by emissions from home heating.

## ARTICLE INFO

*Keywords:*
Biomass burning
Aerosols
Optical properties
Chemical characterization
Wildfires
Ny-Ålesund (Svalbard)

## ABSTRACT

Summer 2019 is remembered as one of the most intense biomass burning (BB) seasons on record for the Northern Hemisphere. During the MOSAiC expedition, a smoke-dominated layer was identified in the upper troposphere over the North Pole region. The origin of this layer remains unclear, and no evidence has been found to indicate the intrusion of such particles into the Arctic Boundary Layer. The main aim of this work was to evaluate if biomass burning events in the summer 2019 were detectable at Gruvebadet Atmospheric Laboratory, close to Ny-Ålesund (Svalbard Islands) during the second half of 2019. This paper proposes an innovative approach to discriminate biomass burning events based on optical measurements combined with chemical analysis and air mass back-trajectories. Monthly background values of optical coefficients were defined using multi-annual (2018–2021) statistics and twelve possible events were identified. Source apportionment through positive matrix factorization (PMF) identified that the biomass burning factor by PMF accounted for only 2% of the total investigated concentration. The specific biomass burning tracers such as levoglucosan and phenolic compounds were compared with optical measurements and with the PMF results. Air mass trajectory analysis revealed that the early summer fires detected at Ny-Ålesund originated mainly from North America, as also confirmed by the presence of BB factor of PMF, levoglucosan and also vanillic species (softwood combustion tracers). In contrast, the chemical composition and air masses analysis of the highest peak detected in early December suggested residential heating as plausible source, further amplified by the onset of the harsh winter season and the expansion of the polar vortex towards mid-latitudes.

## 1. Introduction

The Arctic is a unique environment that is undergoing enormous changes due to a rapid warming in the region (Boyer et al., 2022). It is clear from paleoclimate records and climate model projections that this region is under enormous stress, which is carrying to an increase of warm waters entrance from the Atlantic into the Arctic Ocean, northward advance of the treeline, permafrost thawing and modification to the global atmospheric circulation (Serreze and Barry, 2011). In this fast-changing region, drier conditions and a general increase in mean and maximum air temperatures contribute to

* Corresponding author at: Ca' Foscari University of Venice, Department of Environmental Sciences, Informatics and Statistics, Via Torino 155, Venice, 30172, Italy.
*E-mail address:* simone.pulimeno@unive.it (S. Pulimeno).

https://doi.org/10.1016/j.atmosenv.2024.120336
Received 10 July 2023; Received in revised form 21 December 2023; Accepted 3 January 2024
Available online 5 January 2024

increased wildfire activity (Box et al., 2019), especially in Central Siberia, Northern America, and Canadian boreal forests (Kharuk and Ponomarev, 2017; Veraverbeke et al., 2017; Kasischke and Turetsky, 2006). What scientists typically considered 'fire-resistant' ecosystems (peatlands, tundra bogs) are now frequently hit by wildfires (McCarty et al., 2020). These are carbon-rich soils formed over thousands of years and represent the most carbon-dense ecosystems on our planet - e.g., a northern bog can contain up to ten times as much carbon as a boreal forest (Witze, 2020). Fires cause extensive air pollution by emitting large amounts of primary atmospheric aerosols (mostly black carbon — BC and brown carbon — BrC) and other gaseous species (Evangeliou et al., 2019). Secondary aerosols are also formed in the atmosphere by chemical reactions involving sulfur dioxide, nitrogen oxides, and other chemical species (Tomasi et al., 2017). Primary and secondary aerosol particles interact with shortwave solar radiation differently depending on their size and chemical composition (Iqbal, 1983). Through the absorption and scattering of solar radiation, biomass burning (BB) aerosols can alter the surface energy budget, act as cloud condensation nuclei, and change the cloud albedo (Tomasi et al., 2017). Aerosol optical and chemical properties can strongly fluctuate seasonally as meteorological conditions and sources (natural or anthropogenic, from inside or outside the Arctic region) change in time (Quinn et al., 2008). Shaw (1995) described the Arctic haze phenomenon, defining it as an inflow of polluted air from middle latitudes or an uplift outside the Arctic dominated by accumulation mode aerosols (size between 0.5-2 μm) during winter and spring. Contrariwise, the Arctic troposphere is relatively isolated during the summertime because of the absence of diabatic-surface cooling and the disappearance of high continental pressure (Shaw, 1995; Stohl, 2006). Thus, since the interactions of aerosols with solar radiation are at their maximum during summer, the concentration of light-absorbing aerosol can be very problematic, having the potential to act as a positive feedback mechanism to the Arctic amplification phenomenon (Gillett et al., 2004). The Arctic region is experiencing an increase in biomass burning events, which result in the release of aerosols into the atmosphere with significant impacts on the environment (Stockwell et al., 2015).

Summer 2019 was remembered as one of the most intense burning seasons on record for the northern hemisphere, especially because of the spread of wildfires in Yacutia (Siberia) with an unprecedented magnitude and size, and a total burned area of three million hectares (Voronova et al., 2020). In September 2019, the MOSAiC Expedition started with the German research icebreaker Polarstern drifted through the Arctic Ocean for a year. Throughout the campaign, researchers detected a persistent layer of aged wildfire smoke in the upper troposphere and lower stratosphere (UTLS) (Ohneiser et al., 2021). Furthermore, Lidar observations conducted at Ny-Ålesund revealed an increase in the stratospheric aerosol optical depth (AOD) during the summer period of 2019 (Engelmann et al., 2021). Ohneiser et al. (2021) emphasized that the question of whether the fires in central and eastern Siberia were the source of the smoke observed in the UTLS over the North Pole region during the MOSAiC expedition still remains unanswered. Engelmann et al. (2021) speculated that the smoke was lifted by the so-called self-lifting process to the UTLS. Then smoke particles became quickly distributed over large parts of the Northern Hemisphere within a few weeks.

This paper aims to investigate if the biomass burning occurred in summer 2019 was detectable at Ny-Ålesund (Svalbard) within the Arctic Boundary Layer. Aerosol sampling and measurements were performed at Gruvebadet Atmospheric Laboratory (GAL), close to the research village of Ny-Ålesund, from mid-June to December 2019, coinciding with MOSAiC's report on the presence of a thick 10 km layer of wildfire smoke. In this paper, we present an innovative multidisciplinary approach that combines aerosol optical properties with chemical characterization and source apportionment analysis throughout the entire period to identify events attributable to wildfires. Furthermore, we performed high-resolution back-trajectory analysis to determine the origins of air masses reaching Svalbard lower troposphere.

**Fig. 1.** View of Oscar II Land with the village of Ny-Ålesund on the southern shore of Kongsfjorden. The Gruvebadet Atmospheric Laboratory is marked with a red dot. Retrieved from TopoSvalbard (https://toposvalbard.npolar.no/; accessed May 2023).

## 2. Materials and methods

### 2.1. Area of investigation

Observations of the atmospheric composition, with a particular focus on aerosols, were carried out at the Ny-Ålesund Research Station, on the Spitsbergen Island of Svalbard. The station is placed on the southern shore of Kongsfjorden, and the aerosol in situ measurements, for both optics and chemistry, were made at the Gruvebadet Atmospheric Laboratory (GAL, 78.91°N, 11.89°E; 61 m a.s.l., see Fig. 1) located about 1 km south from the settlement. The location of GAL ensures minimal anthropogenic influence of the village thanks to the dominant wind's regime, oriented along the north-west/south-east direction (Mazzola et al., 2016).

### 2.2. Aerosol optical characterization

Aerosol optical properties have been measured at GAL using a combination of different instruments since 2010. For our purposes, we used measurements collected from January 2018 to December 2021 to describe the average seasonal changes and discuss the variability during the investigated period (second half of 2019). During the period 2018–2021 measurements were continuous along the year and representative of both the cold and the warm seasons. A Radiance Research's M903 nephelometer was used to measure the light scattering extinction coefficient ($b_s$) at 530 nm, while the Particle Soot Absorption Photometer (PSAP), also by Radiance Research, retrieved the amount of light absorbed by the collected particles ($b_a$) at three wavelengths (467, 530, and 660 nm). The nephelometer and PSAP measurements were averaged hourly and corrected following Virkkula (2010). The meld between $b_s$ and $b_a$ at 530 nm allowed the evaluation of Single Scattering Albedo (SSA) at the same wavelength, which gives information about scattering efficiency with respect to total extinction efficiency. In this study it was derived as follows:

$$SSA = \frac{b_s}{b_s + b_a} = \frac{b_s}{b_{ext}} = 1 - \frac{b_a}{b_{ext}} \quad (1)$$

where the $b_s$ is the scattering coefficient, $b_a$ the absorption coefficient, both at 530 nm, and $b_{ext}$ the extinction coefficient given by the sum of scattering and absorption. Furthermore, the $b_a$ at 467 and 660 nm were used to calculate the Absorption Ångström Exponent (AAE) that, such as SSA, is an intensive property of particles which describes the wavelength dependence in aerosol absorption and it is defined as:

$$b_{a(\lambda)} = b_0 \lambda^{-AAE} \quad (2)$$

where $b_{a(\lambda)}$ is the aerosol absorption coefficient, $\lambda$ represents the wavelength, and $b_0$ a wavelength independent constant equal to the absorption coefficient at $\lambda = 1$ μm. AAE usually decreases exponentially with $\lambda$ over the visible and near-infrared spectrum bands (Ångström, 1929). In this manuscript, the Ångström parameter was retrieved as the slope passing through two points. Specifically, it was defined as:

$$AAE = \frac{-log(b_a(467)/b_a(660))}{log(467/660)} \quad (3)$$

where $b_a(467)$ and $b_a(660)$ are the absorption coefficients at wavelength 467 and 660 nm respectively.

Meteorological data were acquired from the Amundsen–Nobile Climate Change Tower (CCT), located about 2 km NW from Ny-Ålesund. The CCT provides continuous profile of meteorological parameters at four levels up to 34 m and, in this paper, data averaged every 30 min at a height of 5 m were used for temperature, relative humidity, wind speed, and wind direction (Mazzola et al., 2016).

For December 2019 only, we present corrected Level 1 Aerosol Optical Depth (AOD) data from AErosol RObotic NETwork (AERONET). At Ny-Ålesund, University of Valladolid and AWIPEV manage a solar–sky–moon CIMEL-318T photometer for the retrieval of AOD at 6 different wavelengths (440, 500, 675, 870, 1020, and 1640 nm) (Sinyuk et al., 2020). Moon-photometers enable the measurements of lunar irradiance and the derivation of AOD and other products also during night-time (Román et al., 2020; González et al., 2020). AOD is a measure of the amount of light scattering and absorption by aerosol particles along the path of the light beam. Because of the Arctic haze phenomenon, AOD in the Arctic is noticeably higher during winter and spring rather than in summer (Tomasi et al., 2015). Because level 1 lunar-AOD data exhibited disturbance due to the presence of clouds, we applied a correction procedure (more information will be provided in Supplementary material)

### 2.3. Aerosol sampling and chemical characterization

Twenty-seven aerosol samples were collected from 16th June 2019 to 2nd January 2020 at the GAL. A multi-stage Andersen impactor (TE-6000 series, Tisch Environmental Inc.) was used to collect aerosol samples on six pre-combusted (4 h at 400 °C in a muffle furnace) quartz fiber filters. The sampler accumulates particles with cut-off diameters of 10 μm, 7.2 μm, 3.0 μm, 1.5 μm, and 0.95 μm on slotted filters and < 0.49 μm on the backup filters. The frequency of sampling varied from 6 to 10 days, for a total air volume of 9000 to 15 000 $m^3$ per sample. Field blanks were obtained using the same filters installed on the sampler with the air pump switched off. Both samples and blanks were wrapped in a double layer of aluminium foil and stored at −20 °C until analysis.

Half of the filter was broken into small pieces and placed in a 50-mL polyethylene vial (previously cleaned with ultrapure water into ultrasonic batch for 30 min) with steel tweezers. The sample was spiked with 50 ng of $^{13}C$-labeled internal standard mix of amino acids, $^{13}C_1$-vanillic acid and $^{13}C_6$-vanillin and 100 ng of $^{13}C_6$-glucose and $^{13}C_6$-levoglucosan. Extraction was carried out in an ultrasonic bath for 30 min with 15 mL and 30 mL of ultrapure water for slotted and back-up filters, respectively. The extract solution was filtered through a 0.45 μm PTFE filter to remove particles and quartz fiber traces before instrumental analysis. Previously validated methods were applied to the aerosol samples to determine inorganic ions and organic acids (methanesulfonic acid and C2-C7 carboxylic acids) (Barbaro et al., 2017; Feltracco et al., 2021), monosaccharides, alcohol-sugars, levoglucosan and its isomers, sucrose (Barbaro et al., 2015a), free amino acids (Barbaro et al., 2015b), phenolic compounds (Zangrando et al., 2016), and photo-oxidation products of α-pinene (Feltracco et al., 2018).

### 2.4. Source apportionment using positive matrix factorization

Positive Matrix Factorization (PMF) method (Paatero and Tapper, 1994) was used to identify the number of factors/sources and their chemical profiles. The model uses data for all concentration and uncertainty values for *j* species and *i* days. Data confidence can be maintained by adjusting the uncertainties by real observations. For the current analysis, the U.S. EPA version of PMF was used (EPA PMF 5.0), which is based on the multilinear engine ME-2. In this study, the input dataset was created by compiling the concentrations of the detected chemical species (variables, n = 27) for each stage of the impactor (6 different sizes) across 27 samples, resulting in a total of m = 6 × 27 = 162 cases. This approach enables the allocation of different stages for assessing the temporal evolution of the samples while considering particle size distribution. The uncertainties in sample concentrations were assessed by considering the relative standard deviation of each variable obtained during the validation procedure. For the PMF application, an additional 10% uncertainty was incorporated for all species. Uncertainties in the PMF results were determined using the bootstrap method. The optimal number of factors was determined by analyzing the parameters IM (maximum individual column mean) and IS (maximum individual column standard deviation) derived from the scaled residual matrix, along with Q-values (goodness-of-fit parameters). Specifically, for Q-values, the optimal solution was identified at the point where the curve's slope exhibited a significant change. Conversely, for the IM and IS parameters, as the number of factors increased to a critical value, these parameters experienced a sharp decline. In this work, the values of Q, IM, and IS indicated a reasonable solution corresponding to 5 factors.

### 2.5. Satellite data and back-trajectory analysis

Satellite-derived fire data were obtained from the Fire Information for Resource Management System (FIRMS) active fire detection product of the Moderate Resolution Imaging Spectroradiometer (MODIS) instrument onboard the Terra and Aqua satellites. The data were obtained from the online platform FIRMS (https://firms.modaps.eosdis.nasa.gov; accessed March 2023) and cover the whole period from June to December 2019. Satellites capture a snapshot of Earth's surface as they orbit. These images contain hotspots that correspond to the center of pixels of approximately 1 km, flagged as containing thermal anomalies. To measure the brightness temperature of a hotspot, which is a measurements for the photons received by the spacecraft at a specific wavelength, FIRMS uses the MODIS channels 21/22 and 31. In this work we utilized the Fire Radiative Power (FRP) parameter from the MODIS data to create maps of active fires for each identified BB event. The FRP (W) represents the rate of radiant energy released by a fire, and is a useful parameter to estimate the fire intensity and burned area. By using the FRP data, we were able to accurately locate and visualize the active fire spots.

To identify possible sources of BB particles reaching the sampling site, we used the HYSPLIT model developed by the National Oceanic and Atmospheric Administration (NOAA) Air Resource Laboratory. HYSPLIT is a widely used tool for air mass trajectory analysis that can be used to simulate the trajectory of air masses based on meteorological data from the Global Data Assimilation System (GDAS). Using HYSPLIT, and in particular Global Forecast System (GFS) data at 0.25 degrees, we generated 240-h back-trajectory frequency plots for air masses arriving at Ny-Ålesund, with a time step of 1 h (24 trajectories per day). The starting height of the trajectories was set at 50 m above ground level. The back-trajectory frequency plots show the parts of back-trajectories below the mixing height for different receptor locations. The plots were generated by dividing the region of interest into a grid of cells and counting the number of back-trajectories endpoints within the boundary layer in each cell. The frequency provided information about the potential areas of origin of the aerosol burning particles during

extreme events. Overall, HYSPLIT back-trajectory analysis provided valuable insights into the transport patterns of aerosol burning particles during extreme events and helped us to identify the possible areas of origin of these particles.

### 2.6. NAAPS transport model

To identify the origin of BB smoke and assess the concentration of aerosols at Ny-Ålesund, the Navy Aerosol Analysis and Prediction System-Reanalysis (NAAPS-RA) has been employed. NAAPS is the US Navy's chemical transport model, operating at a spatial resolution of 1 × 1° with data updated every 6 h, providing information on aerosol optical depth at 550 nm. This information is primarily based on the Danish Eulerian Hemispheric Model (Witek et al., 2007). The NAAPS model has the capability to characterize various types of aerosols, including biogenic and anthropogenic particles, sea salt, dust, and BB smoke. Specifically, in the case of BB smoke, it relies on near-real-time satellite-based thermal anomaly data to construct smoke source functions. In NAAPS reanalysis, additional orbital corrections for MODIS-based emissions are applied, and a two-day maximum approach (considering signals from the previous day and the present day) is utilized to minimize orbital effects (Lynch et al., 2016). This approach enables the accurate identification of the sources of BB smoke and the assessment of aerosol concentration in Ny-Ålesund, contributing to a better understanding of aerosol transport and its impact on the region. To gain a more in-depth knowledge of the aerosol plume's dynamics, please refer to the NAAPS animation provided at this link: https://youtu.be/5lXQU9HzSBU.

## 3. Results

The results section of this study provides a detailed analysis about the optical and chemical properties of aerosols detected at Ny-Ålesund during the latter half of 2019. Our findings present insights into the main characteristics, source areas, and transport of these events on the local and regional atmosphere. Through the use of aerosol characterization techniques, we have identified the optical properties and chemical composition of these aerosols, allowing for a better event detection.

### 3.1. Optical properties and events detection

Identifying biomass burning events from aerosol optical properties remains a challenge, particularly in the Arctic, where other sources of aerosols, long-range transport, and particle aging processes can further complicate the analysis (Kyrö et al., 2013). While a well-defined procedure for such identification is not available, previous studies have attempted to identify wildfires using various aerosol optical parameters (Markowicz et al., 2016; Stohl et al., 2013; Dall'Osto et al., 2019; Zielinski et al., 2020). These studies typically rely on ground-based measurements and air mass trajectory analysis to confirm the source of aerosol particles. Scattering and absorption coefficients at 530 nm, from January 2018 to December 2021, are shown in Figure S1. During the winter–spring months, frequent episodes of high scattering and absorption values were observed at Ny-Ålesund, with maximum values of almost 48 $Mm^{-1}$ and 5 $Mm^{-1}$, respectively, with events lasting from a few hours to few days. In line with previous studies, the mean (and median) value of $b_s$ and $b_a(530)$ were found to be 3.63 (2.40) $Mm^{-1}$ and 0.22 (0.13) $Mm^{-1}$, respectively. Specifically, Schmeisser et al. (2018) reported similar annual statistical values of 4.35 (2.82) $Mm^{-1}$ and 0.18 (0.09) $Mm^{-1}$ for scattering and absorption coefficients at the same location for years 2012–2014.

We obtained multi-annual monthly means of $b_s$ and $b_a$ from this 4-years time-series, which are presented in Fig. 2. There is a clear seasonality for both parameters, consistent with findings from other studies (Pandolfi et al., 2018; Schmeisser et al., 2018). Specifically, aerosol scattering and absorption exhibit a significant peak during late winter–spring, which coincides with the Arctic haze phenomenon, due to the effective transport from the lower latitudes (Gilardoni et al., 2023). The monthly averages of $b_s$ between February and April ranged from 4.74 to 6.04 $Mm^{-1}$, representing the highest values observed. Conversely, the summer months exhibited minimum values of approximately 2.44–2.57 $Mm^{-1}$ for this parameter. Similarly, $b_a(530)$ displayed the highest values during late-winter and early-fall months, ranging from 0.32 to 0.40 $Mm^{-1}$, while the summer months exhibited the minimum values in the range of 0.09–0.15 $Mm^{-1}$. Throughout our study, we found that a log-normal frequency distribution accurately fits the data for both coefficients. Interestingly, the mean values were consistently higher than the median for all months. As a way to establish a baseline for our analysis, the multi-annual monthly statistics were evaluated (thus including the 5th, 25th, 50th, 75th, 95th percentile, and mean) in order to identify the most appropriate monthly background values for each coefficient (Fig. 2). Table 1 shows the statistical values for the months of June–December, as they were used to assess the anomalies for the same period of 2019. Selecting a background value is crucial to accurately assess the contribution of BB events to the observed aerosol properties. In this work, the 50th percentile has been used as the background value for $b_a$ during the identification of events, since it helps to minimize the influence of extreme values and outliers.

**Table 1**
Means of $b_a(530)$ at Ny-Ålesund, including 25th, 50th, and 75th percentile calculated for each month from June to December based on 4-years of data (2018–2021).

| Month | 25th | Mean | 50th | 75th |
|---|---|---|---|---|
| June | 0.03 | 0.11 | 0.06 | 0.14 |
| July | 0.03 | 0.14 | 0.08 | 0.17 |
| August | 0.04 | 0.16 | 0.10 | 0.21 |
| September | 0.02 | 0.09 | 0.06 | 0.13 |
| October | 0.02 | 0.07 | 0.04 | 0.09 |
| November | 0.04 | 0.14 | 0.10 | 0.19 |
| December | 0.07 | 0.23 | 0.15 | 0.28 |

We focused on events that exceeded the 50th percentile of the reference month for at least 12 h per day and for a minimum of two consecutive days. This criterion has been adopted to differentiate extreme wildfire events from short-term absorption spikes that may originate from local sources or transient events. By using this criterion, identify 12 long-lasting BB events and ensure that they were not merely artifacts caused by short-term variability in the measurements (Table S1).

### 3.2. Aerosol chemical composition and PMF analysis

Biomass burning tracers, such as levoglucosan, its isomers and phenolic compounds were determined in the aerosol samples collected at GAL from mid-June to the end of December 2019 with low temporal resolution (6–10 days) compared to optical measurements (1 h). Moreover, other chemical tracers (inorganic ions, organic acids, free amino acids and sugars) were investigated to perform a complete characterization of aerosol and to identify their sources.

The most abundant species (Table S2) were sulphate (40%), chloride (23%) and sodium (21%), while ammonium (4%), magnesium (3%), calcium (3%) and nitrate (3%) were below 5%. All other investigated species are below 1%. Sodium, chloride, and magnesium are the main components of the sea spray source (Giardi et al., 2016), whereas non-sea salt fraction of $Ca^{2+}$ and $SO_4^{2-}$ represented 72% and 86%, respectively. The contributions of the non-sea-salt fraction of $Ca^{2+}$ and $SO_4^{2-}$ were calculated for the difference between their concentrations and the sea salt values obtained using the $Ca^{2+}/Na^+$ ratio in seawater (0.038 w/w) and the $SO_4^{2-}/Na^+$ ratio (0.252 w/w). The particle size distribution of major ions (Figure S3a) confirmed the local sources of sea salt components because $Na^+$, $Cl^-$ and $Mg^{2+}$ were mainly distributed in the coarse mode. The most abundant species was sulphate and several sources can emit this ion. The sea-salt sulphate ($ss-SO_4^{2-}$)

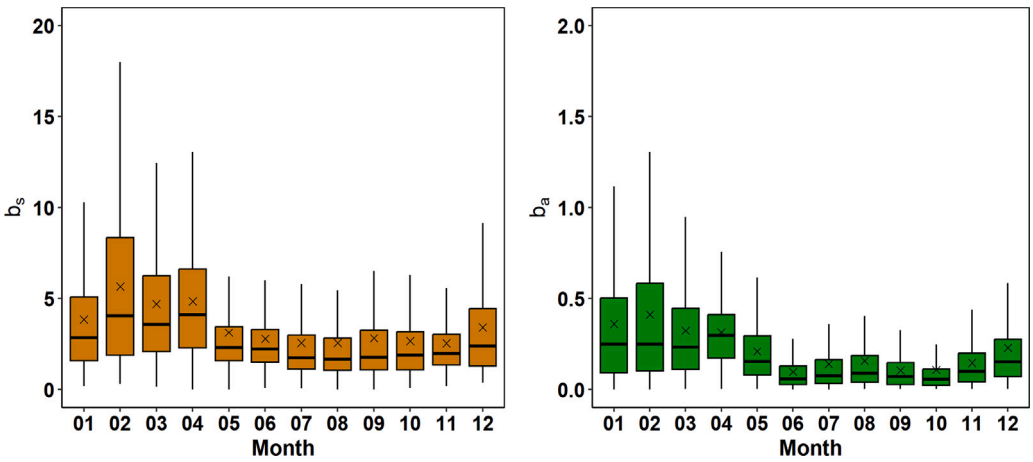


**Fig. 2.** Monthly box-and-whisker plots of $b_s$ and $b_a(530)$ obtained from hourly data over the period 2018–2021 at Ny-Ålesund. Each plot shows the 5, 25, 50 (median), 75, and 95th percentiles, as well as the mean value (cross) for each month.

contributed minimally (14±7%) to the sulphate budget and exhibited an increase during the winter period, whereas the main sources were attributed to anthropogenic sources due to the atmospheric oxidation of $SO_2$ (Udisti et al., 2016). In fact, we evaluated also crustal components and the sulphate contribution from marine phytoplanktonic activity as suggested by Udisti et al. (2016) but these contributions are lower considering the total non-sea-salt sulphate (Figure S3b). The phytoplanktonic contribution has an increase during the summer period linked to the algal bloom (Becagli et al., 2019).

The total median concentration of carboxylic acids is 4 ng $m^{-3}$ and $C_2$-oxalic acid (48%) and acetic acid (21%) are the most abundant carboxylic acids. The sugars composition is dominated by levoglucosan (32% of the total median concentration of sugars), glucose (19%), mannitol (16%) and arabitol (11%), two tracers of fungal spores. The median concentration of L-free amino acids is 202 ng $m^{-3}$, with L-arginine (36%) of the total median concentration of 20 ng $m^{-3}$ with the only presence of D-alanine and D-aspartic acid. Finally, the main components of organic acids are the phenolic compounds with vanillin moieties, the main products of the combination of softwood, and two photo-oxidation products of $\alpha$-pinene (cis-pinonic and pinic acids).

The comparison of aerosol concentrations reconstructed by the PMF and those measured showed that the PMF can reconstruct the data with a slope of 0.99 and an $R^2$ of 0.91. The profile of each factor, in terms of concentrations (bars) and in terms of percent of species (black points), the temporal trend and the particle size distribution of each factor are shown in Fig. 3.

The first factor (F1) describes 51% of the total investigated concentration, and it is mainly characterized by saline ions. $Na^+$ and $Cl^-$, that are recognized as specific tracers of sea salt aerosol (O'Dowd et al., 1997), suggest that this factor represents the sea spray component. Moreover, the particle size distribution (Fig. 3C) defines that this first factor is mainly distributed on the coarse mode, confirming a local marine source of this type of aerosols. The general trend of sea salt factor (Fig. 3B) shows an increase starting in autumn due to more frequent cyclonic system. Sea salt emissions from sea-ice due to blowing snow reach their maximum in December (Huang and Jaeglé, 2017).

The second factor (F2), loaded for 30% of the total investigated concentration, is called "sulphate and long range compounds" because sulphate is the most abundant species but other organic compounds with long range transport sources are well represented in this factor. For example, photo-oxidation products of $\alpha$-pinene (cis-pinonic and pinic acids), glycolic and maleic acids and also levoglucosan are included in this factor (Fig. 3A). It consists mainly of fine aerosols and does not show a seasonal trend in the considered period.

The third factor (F3) describes the 12% of the total concentration estimated by PMF, and it loads with methanesulfonic acid (MSA), carboxylic acids and pinonic acid (Fig. 3A). These species are the secondary photo oxidation products, mainly distributed on the fine particles (Fig. 3C). Moreover, Fig. 3B well shows that these species have higher concentration until the end of July, which then drops dramatically.

The fourth factor (F4), loaded for 5%, is characterized by arabitol and mannitol, with also glucose and L-free amino acids. This factor represents the biogenic emission from fungal spores, occurred during the summer period (Fig. 3B) and it is mainly distributed on the coarse fraction (Fig. 3C).

Finally, the last factor (F5) represents the "biomass burning contribution" because levoglucosan characterizes it, with also a contribution of L- and D-free amino acids and oxalic acid. This factor is mainly distributed on the fine particles suggesting a source of atmospheric long-range transport. For the aim of this work this is the most important factor, but it loads only for 2% of the total investigated concentration.

## 4. Discussion

Fig. 4 shows in situ surface optical observations for the period June–December 2019, plotted as daily averages. Despite some data gaps, our analysis reveals variable values of $b_s$ and $b_a$, at all wavelengths, throughout most of the season. These values contrast with the relatively stable $b_s$ and $b_a$ coefficients observed during September and October 2019, which are consistent with values reported by other authors (Zielinski et al., 2020). Specifically, $b_s$ was found to be around 2 $Mm^{-1}$, while $b_a$ was lower than 0.07 $Mm^{-1}$. In Fig. 4, it can be observed that between June and September, AAE values typically fell within the range of 1 to 2, displaying relatively limited variation. During this period, there was also a decrease in the SSA value. In contrast, in the months from October to December, higher and more widely dispersed AAE values were observed, while the SSA value remained relatively stable at around 1.

After comparing such observations with multi-annual monthly means values determined through the procedure described in Section 3.1, twelve events were detected by the analysis of aerosol optical parameters (Table S1).

A careful analysis revealed that from the middle of June, when also chemical analysis was performed, only narrow peaks of $b_a$ were detected until the end of July. However, data were missing for about two weeks from the end of June to the beginning of July. Despite the missing data, Figure S2 shows that $b_a(530)$ levels exceeded the monthly background value of June and July (0.03 $Mm^{-1}$, see Table 1) for two periods, June 19–22 and July 29–30, with peaks reaching about 0.6 $Mm^{-1}$ and 0.5 $Mm^{-1}$, respectively. Based on the back-trajectory frequency plots (Figure S4), the first episode is plausibly linked to

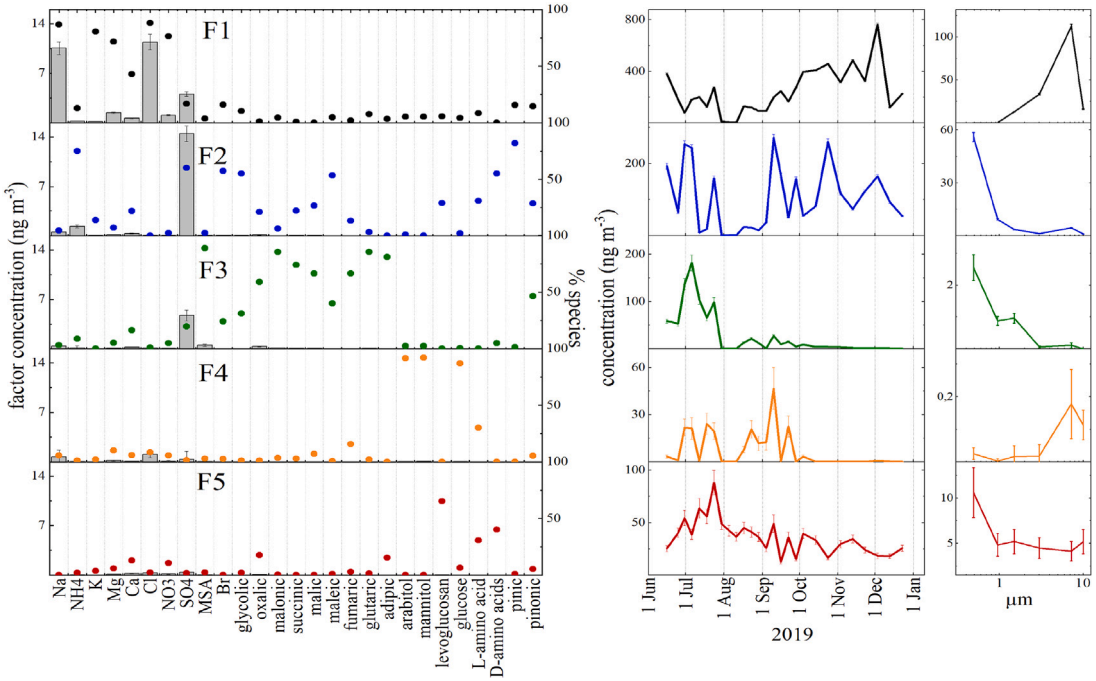


**Fig. 3.** Results of Positive Matrix Factorization (PMF); (A) source profiles where bars identify the species in ng $m^{-3}$ that mainly characterize each factor (F1 — sea salt input; F2 — sulphate component and long range compounds; F3 — secondary products; F4 — fungal spores; F5 — biomass burning) profile while the points describe the percent of species; (B) factor contributions during the sampling period; (C) particle size distribution of each factor.

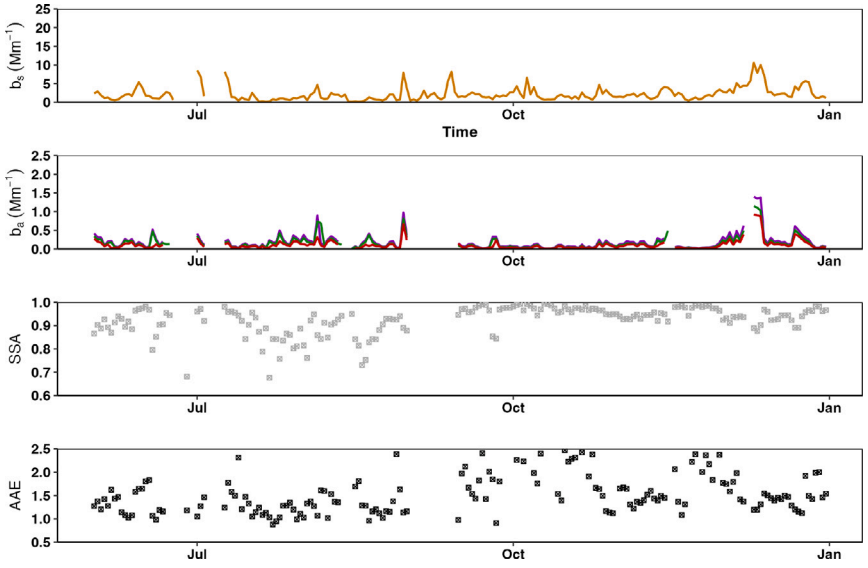


**Fig. 4.** Daily aerosol optical parameters taken between June and December 2019. The upper panel shows scattering coefficient, while the middle panel displays absorption coefficients (467 nm in violet, 530 nm in green, and 660 nm in red). The bottom panel represents the AAE (black) and the SSA (gray), retrieved with $b_a$ values higher than 0.07 $Mm^{-1}$.

the mid-June fires that occurred in the Canadian provinces of Alberta and Saskatchewan as well as in the northeastern regions of the United States. Considering the chemical analysis of wildfire tracers, aerosol seems not affected by BB events during June, probably due to the intensity of fires or weak transport processes.

For the late July event the air masses appear to have originated from both Canada and Alaska. From the end of July to the beginning of August, the wildfire afflicted mainly the North America and Siberia. The back-trajectories analysis showed that air masses weakly come from North America and then remain steady over the Svalbard archipelago. According to the wind direction analysis conducted using data from CCT (not shown), during this period a significant portion of air masses sampled at GAL was found to come from the E and NE (town center). This suggests that the pollution event observed in early August may be attributed to a local source of pollution. However, Fig. 5 reports a value of almost 50 ng $m^{-3}$ for factor 5 by PMF, and spikes in the levoglucosan trend (almost 0.25 ng $m^{-3}$), vanillin (VAH, 0.05 ng $m^{-3}$), vanillic acid and acetovanillone (VA and VAC respectively, approximately 0.003 ng $m^{-3}$). The presence of such wildfire tracers, which are specific markers of conifer fires, seems to point out a long-range transport rather than a local influence despite the air masses being stable over the Svalbard archipelago. Furthermore, LIDAR measurements at Ny-Ålesund indicate

a strong increase in the upper troposphere and lower stratosphere AOD in August 2019, suggesting the occurrence of long-range transport processes (Ohneiser et al., 2021).

Whereas the evaluation of events in the summer period was quite straightforward, during autumn the constrains of our approach seem to minimize some episodes. In particular, throughout the period August–December 2019, discernible spikes were observed that could potentially suggest the occurrence of biomass burning events. Nonetheless, the established criteria (exceeding the 50th percentile for at least 12 h) for identifying events were not satisfied by these observations and consequently, these spikes were not included in our analysis. The majority of the events identified using our approach mainly occurred during the fall and early-winter months. During the late summer — early fall, aerosol scavenging along the pathways from lower latitudes to the Arctic decreases compared to previous months, leading to a more efficient transport of polluted air masses and the consequent increase in aerosol scattering and absorption coefficients (Gilardoni et al., 2023; Garrett et al., 2011). This may account for the high number of events identified between September and December 2019 in our study. Moreover, Figure S4 shows an evident change of atmospheric transport regime, mainly from North America during the summer period to North Europe and Russia during autumn and early-winter.

In general, the increase in the aerosol absorption coefficient was not accompanied by a proportional increase in the scattering coefficient. This behavior indicates a shift towards a higher fraction of absorbing particles, likely caused by the presence of BB aerosols in the atmosphere. Accordingly, the SSA exhibited a decrease, with values dropping below 0.90 from an average background value of 0.95. In agreement with prior studies, there is a strong correlation between BB emissions and an increase in the aerosol absorbing coefficient at all wavelengths (Eck et al., 2003; Markowicz et al., 2016; Zielinski et al., 2020). The AAE values during the duration of the events are also consistent with the expected values of a burning event, with values tending to lay between 1 and 1.5. (Markowicz et al., 2016). For most of the events identified, the analysis of the aerosol optical properties alone appears to trace them back to the presence of particles attributable to fires, even if additional chemical information is needed to confirm this source.

In general, the mode of representing back trajectories based on frequencies (Figure S4) makes the main sources more legible when dealing with a large number of trajectories, as in our case. However, this type of graph emphasizes converging areas because, unless there is a prevailing current throughout the period, it is evident that as one moves away from the arrival point, the paths diverge. This implies that the frequency density decreases as one moves away from the source region, which is why a logarithmic scale was used. It is also the reason why the highest values are generally observed at the receptor site, which is furthermore always within the Planetary Boundary Layer (PBL). This discussion suggests that there might have been regions through which only a few trajectories passed, but they could have been significant in terms of collected material. However, such regions were not revealed by the frequency graph, and this could have been particularly true for the events that occurred on 19–22 June, 29–30 July, and 09–10 August. An animation has been created by merging daily NAAPS-RA smoke AOD distribution plots to illustrate the smoke transport path from June to December 2019 (https://youtu.be/5lXQU9HzSBU). The NAAPS-RA data reveal a noteworthy increase in AOD in the Arctic, spanning from mid-June to early September. Fires originating in Siberia, Canada, and Alaska were identified as the sources responsible for the transported BB smoke, as measured at Ny-Ålesund, specifically on July 29–30 and during all the episodes recorded in August. Since the beginning of September no discernible active hot spots have been recorded. The PMF analysis was performed including major ions, MSA, carboxylic acids, levoglucosan, arabitol and mannitol, glucose, L- and D-amino acids and pinic and pinoic acids. $Na^+$, $Cl^-$, and $Mg^{2+}$ are originated by sea spray; conversely, $Ca^{2+}$, $K^+$, and $SO_4^{2-}$ have relevant contributions from other sources, especially crustal aerosol and anthropogenic/biogenic emissions (Amore et al., 2022). MSA is originated by the atmospheric oxidation of dimethyl sulphide (DMS), emitted by phytoplankton (Udisti et al., 2016), while carboxilic acids are considered secondary organic aerosol (SOA) and they can have several sources, as recently demonstrated by Feltracco et al. (2021). A limited number of sugars are included in the PMF analysis to reduce the noise during the modeling: arabitol and mannitol were selected as fungal spore's tracers, glucose is a biogenic compound but it is not specific as tracer, while as already pointed out levoglucosan is the key indicator for biomass burning emissions. The source apportionment approach gave a reasonable solution with five factors.

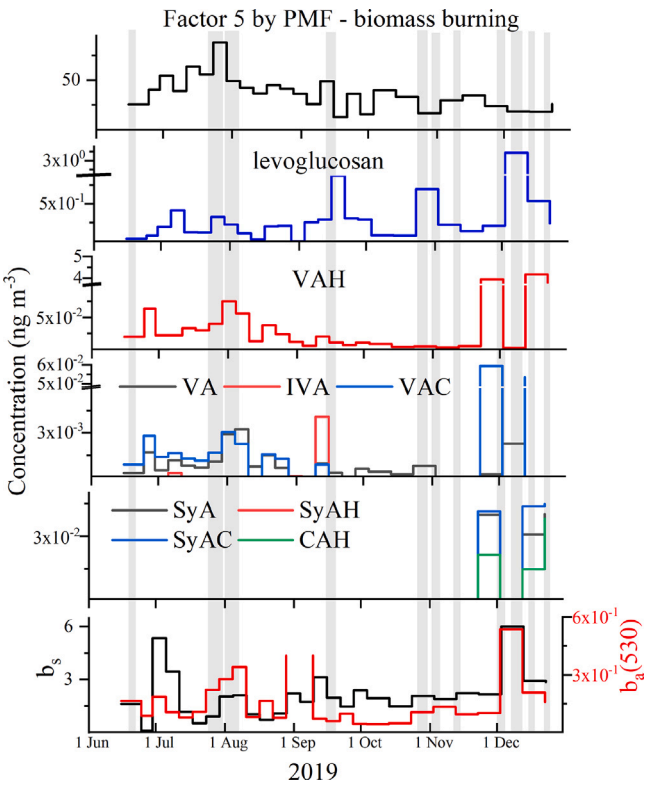


**Fig. 5.** Trends of factor 5 by PMF, levoglucosan, phenolic compounds in $PM_{10}$ samples, and scattering and absorption coefficient at 530 nm ($Mm^{-1}$) collected at GAL from June to December 2019. The shaded vertical stripes refer to the event reported in Table S1.

Fig. 5 shows the comparison between aerosol optical properties and chemical analysis. In particular, the fifth factor of PMF, attributed to BB contribution, and wildfire tracers, such as levoglucosan and phenolic compounds, are included in the Fig. 5. There is a good agreement between optics and chemistry for the events occurred at the end of July and the beginning of August. The elevated values observed in absorption and scattering align well with the peaks in PMF and the chemical analysis of aerosol samples collected at GAL. As depicted in Fig. 5, PMF factor 5 struggles to fully capture the peak associated with BB in December, primarily due to its low factor loading, which is only 2%. Nonetheless, the events identified in early December were of particular interest owing to their very high measurements in both optical properties and chemical composition, along with the timing of their occurrence. The presence of BB events is substantiated by chemical tracers, with the most prominent peaks observed in levoglucosan (3 ng $m^{-3}$) and vanillic acid (0.003 ng $m^{-3}$), both of which are specific markers of combustion.

Fig. 6 presents a detailed view of the aerosol optical properties for the early December events. With a high temporal resolution of 1 h, it was possible to identify two different episodes: the first occurring

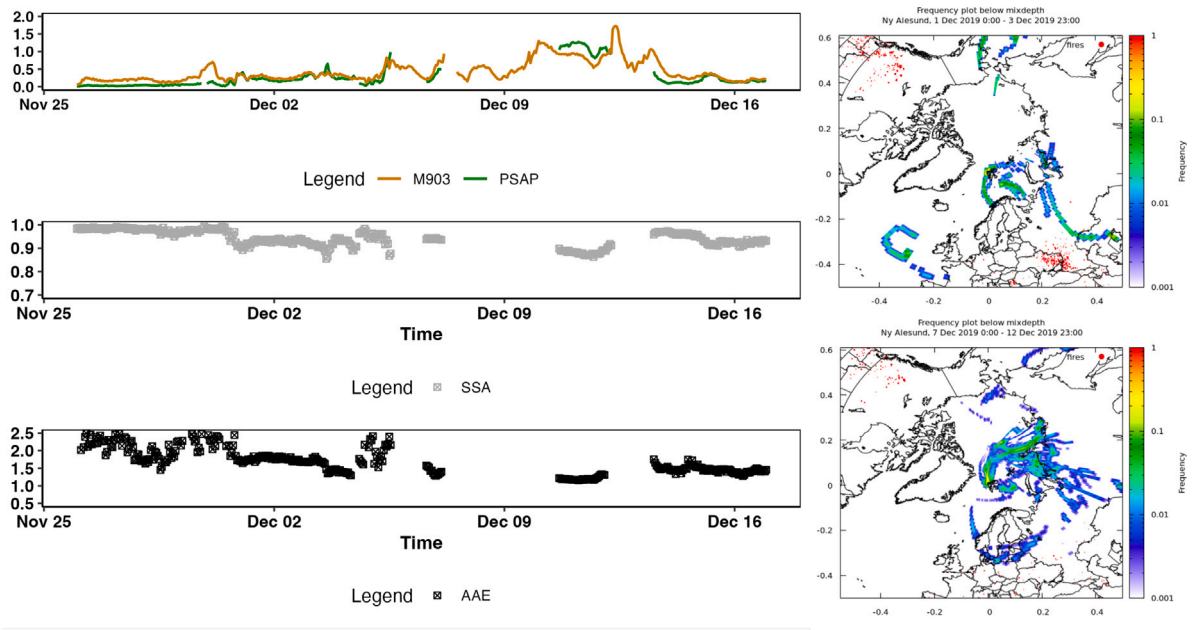


**Fig. 6.** Hourly aerosol parameters for the early December events; $b_s$ acquired from nephelometer M903, and $b_a(530)$ from PSAP are shown in the upper left panel, while SSA and AAE are shown in the lower left panel. The upper right and lower right panels illustrate the back-trajectory frequency plots below the mixing height for the first and second early December events, respectively.

between December 1 and 3, and the second between December 7 and 12. It can be observed that the scattering and absorption coefficients remained relatively stable until the beginning of December (around 2.3 $Mm^{-1}$ for $b_s$ and 0.06 $Mm^{-1}$ for $b_a$ at 530 nm). During both these events, the SSA exhibited a significant decrease dropping to values close to 0.90. On the other hand, AAE provided limited information due to the scarcity of data and the presence of scattered values. Nevertheless, during the two early December episodes, the AAE values appear to be in the range of 1.3 and 1.7, indicating a potential contribution of biomass burning to the aerosol mix. The intensity of these events during December were considered anomalous, and it may suggest a local influence from Ny-Ålesund. However, to verify this hypothesis, we referred to Figure S5, which includes the AOD trend measured by the CIMEL photometer installed at the AWIPEV observatory. In Figure S5, it can be observed that data were not available for the first early-December event (December 1 to 3). However, for the second event, an increase in AOD was evident across all wavelengths. The AE values, which ranged between 1 and 1.5, suggest the presence of fine-mode aerosol particles, such as those originating from biomass burning. During both these episodes, the air masses were transported towards Svalbard from Russia, as revealed by the air mass back trajectory analyses. Given the high contribution of other wildfire tracers, such as vanillic compounds, coniferyl aldehyde (CAH), syringic acid (SyA), syringaldehyde (SyAH) and acetosyringone (SyAC) (as shown in Fig. 5), it is probable that the early December episodes were caused by a mixture of sources. MODIS data-derived images reveal the presence of active fires in southern Russia, Georgia, and Azerbaijan. Nonetheless, the intensity and duration of these fires were inadequate to account for the high values observed in both the physical and chemical properties of the aerosols. Corroborating this, the NAAPS-RA did not highlight any active fires resulting in BB smoke influence during December. Thus, besides biomass fires, we propose an additional contribution from domestic heating. Additional information about the vertical aerosol structure during these events, and a comparison with Zeppelin station (managed by Norwegian Polar Institute and located on the Zeppelin mountain at 472 m a.s.l. at Ny-Ålesund) could provide new insight into this matter.

## 5. Conclusions

Although the MOSAiC campaign provided evidence of a thick aerosol layer in the UTLS with a clear wildfire smoke signature, the hourly mean values of $b_s$, $b_a$, SSA, and AAE obtained near the ground-level at GAL from mid-June to the end of December 2019 did not exhibit any notable peak events. The analysis of the measurements highlighted the seasonality of aerosol optical properties, showing that $b_s$ ranges mainly from 0 to 25 $Mm^{-1}$ throughout the investigated period, and $b_a(530)$ values were mainly lower than 0.03 $Mm^{-1}$ in summer (for background) and appreciably higher during the winter–spring period (up to 0.07 $Mm^{-1}$ in December). While the SSA time series is consistent with the trend we expected, with an average of 0.95 that drops and stays around 0.90 with the arrival of highly absorbing particles like BB-ones, the AAE trend is often too scattered to derive useful information, with only some exceptions when it assumes values in line with BB particles between 1 and 1.5. The investigation of aerosol optical properties provided the identification of 12 mild pollution events. The back-trajectory analysis indicated that the air masses predominantly originated from North America between June and August. Subsequently, a change in atmospheric circulation patterns led to a shift in the source area towards the Euro-Asian continent.

Chemical characterization of each event was carried out, together with a positive matrix factorization analysis, allowing for the identification of five different factors. The PMF analysis indicates that sea salt is the major contributor in the coarse fraction of aerosol (51%), while long-range atmospheric transport and anthropogenic sulphate deeply contribute (31%) to the fine mode. Secondary organic aerosols, including MSA and small organic acids, were predominantly observed in the fine particles during the light period. Conversely, another factor identified through PMF analysis exhibited fungal spore markers, with higher concentrations found in the coarse particles during the summer season. During the summer season, the notable presence of biogenic particles, including free amino acids and organic acids, was observed in both the coarse and accumulation modes. Further investigation is warranted to explore the potential role of these findings in cloud formation. The final factor (F5), representing the contribution of biomass burning, accounted for only 2% of the total investigated concentration.

It primarily consisted of specific biomass burning tracers, including levoglucosan, L- and D-free amino acids, and oxalic acid. This factor was predominantly associated with fine particles, indicating long-range transport.

Back-trajectory analysis, combined with MODIS data, revealed a weak correlation between active fires and optical and chemical measurements, implying the presence of highly aged particles (i.e., over 10 days old) over Svalbard from November to December. This finding is consistent with the existence of a layer of aged plume over the North Pole region during the same period as observed during the MOSAiC campaign (Engelmann et al., 2021; Boyer et al., 2022). Moreover, the latest events identified in December may have been influenced by emissions from home heating, given the onset of the winter season and the southward expansion of the polar vortex.

The primary outcome of this paper is the establishment of a multidisciplinary approach that integrates optical and chemical data with back-trajectory analysis. The synergy between optical and chemical measurements can effectively distinguish biomass burning events, even if any alteration in the evaluation criteria will inevitably impact the number of detected events. Therefore, careful consideration must be given to the selection and manipulation of these parameters to ensure accurate identification of wildfires.

## CRediT authorship contribution statement

**Simone Pulimeno:** Conceptualization, Data curation, Formal analysis, Investigation, Methodology, Supervision, Validation, Visualization, Writing – original draft, Writing – review & editing. **Federica Bruschi:** Formal analysis, Investigation. **Matteo Feltracco:** Conceptualization, Data curation, Investigation, Validation, Visualization, Writing – review & editing. **Mauro Mazzola:** Conceptualization, Investigation, Methodology, Supervision, Visualization, Writing – review & editing. **Stefania Gilardoni:** Data curation, Formal analysis, Investigation, Writing – review & editing. **Stefano Crocchianti:** Formal analysis, Investigation, Writing – review & editing. **David Cappelletti:** Methodology, Visualization, Writing – review & editing. **Andrea Gambaro:** Funding acquisition, Supervision, Writing – review & editing. **Elena Barbaro:** Formal analysis, Funding acquisition, Investigation, Supervision, Validation, Visualization, Writing – review & editing.

## Declaration of competing interest

The authors declare the following financial interests/personal relationships which may be considered as potential competing interests: Elena Barbaro reports financial support was provided by Government of Italy Ministry of Education University and Research.

## Data availability

Data will be made available on request.

## Acknowledgment

The authors would like to express their acknowledgment to AERONET PIs Christoph Ritter, Victoria E. Cachorro Revilla, Carlos Toledano, and David Mateos for the use of AOD data. The scientific activity in Ny-Ålesund was carried out in the framework of the National Research Council of Italy (CNR) polar program. Logistical support of the CNR-Institute of Polar Sciences (CNR-ISP) is gratefully acknowledged. We want to thank all colleagues at the CNR Dirigibile Italia Arctic Station who worked during the field campaign. The authors gratefully acknowledge the NOAA Air Resources Laboratory (ARL) for the provision of the HYSPLIT transport and dispersion model and READY website (http://www.ready.noaa.gov) used in this publication. We acknowledge the help of ELGA LabWater in providing the PURELAB Pulse and PURELAB Flex.

## Funding

This research was funded by the Italian Ministry of University and Research (MIUR) within the framework of the Arctic Research Program of Italy of the project “BETHA-NyÅ” - Boundary layer evolution through harmonization of aerosol measurements at Ny-Ålesund research station (PRA2021-0020).

## Appendix A. Supplementary data

Supplementary material related to this article can be found online at https://doi.org/10.1016/j.atmosenv.2024.120336.

## References

Amore, A., Giardi, F., Becagli, S., Caiazzo, L., Mazzola, M., Severi, M., Traversi, R., 2022. Source apportionment of sulphate in the High Arctic by a 10 yr-long record from Gruvebadet Observatory (Ny-Ålesund, Svalbard Islands). Atmos. Environ. 270, 118890.

Ångström, A., 1929. On the atmospheric transmission of sun radiation and on dust in the air. Geogr. Ann. 11, 156–166, Publisher: [Wiley, Swedish Society for Anthropology and Geography].

Barbaro, E., Kirchgeorg, T., Zangrando, R., Vecchiato, M., Piazza, R., Barbante, C., Gambaro, A., 2015a. Sugars in Antarctic aerosol. Atmos. Environ. 118, 135–144.

Barbaro, E., Zangrando, R., Padoan, S., Karroca, O., Toscano, G., Cairns, W., Barbante, C., Gambaro, A., 2017. Aerosol and snow transfer processes: An investigation on the behavior of water-soluble organic compounds and ionic species. Chemosphere 183.

Barbaro, E., Zangrando, R., Vecchiato, M., Piazza, R., Cairns, W.R.L., Capodaglio, G., Barbante, C., Gambaro, A., 2015b. Free amino acids in Antarctic aerosol: potential markers for the evolution and fate of marine aerosol. Atmos. Chem. Phys. 15 (10), 5457–5469, Publisher: Copernicus GmbH.

Becagli, S., Amore, A., Caiazzo, L., Iorio, T., Sarra, A., Lazzara, L., Marchese, C., Meloni, D., Mori, G., Muscari, G., Nuccio, C., Pace, G., Severi, M., Traversi, R., 2019. Biogenic aerosol in the arctic from eight years of MSA data from Ny Ålesund (Svalbard Islands) and Thule (Greenland). Atmosphere 349 (10).

Box, J.E., Colgan, W.T., Christensen, T.R., Schmidt, N.M., Lund, M., Parmentier, F.-J.W., Brown, R., Bhatt, U.S., Euskirchen, E.S., Romanovsky, V.E., Walsh, J.E., Overland, J.E., Wang, M., Corell, R.W., Meier, W.N., Wouters, B., Mernild, S., Mård, J., Pawlak, J., Olsen, M.S., 2019. Key indicators of Arctic climate change: 1971–2017. Environ. Res. Lett. 14 (4), 045010, Publisher: IOP Publishing.

Boyer, M., Aliaga, D., Pernov, J., Angot, H., Quéléver, L., Dada, L., Heutte, B., Dall'osto, M., Beddows, D., Brasseur, Z., Beck, I., Bucci, S., Dütsch, M., Stohl, A., Laurila, T., Asmi, E., Massling, A., Thomas, D., Nøjgaard, J., Jokinen, T., 2022. A Full Year of Aerosol Size Distribution Data from the Central Arctic under an Extreme Positive Arctic Oscillation: Insights from the MOSAiC Expedition.

Dall'Osto, M., Beddows, D.C.S., Tunved, P., Harrison, R.M., Lupi, A., Vitale, V., Becagli, S., Traversi, R., Park, K.-T., Yoon, Y.J., Massling, A., Skov, H., Lange, R., Strom, J., Krejci, R., 2019. Simultaneous measurements of aerosol size distributions at three sites in the European high Arctic. Atmos. Chem. Phys. 19 (11), 7377–7395, Publisher: Copernicus GmbH.

Eck, T.F., Holben, B.N., Reid, J.S., O'Neill, N.T., Schafer, J.S., Dubovik, O., Smirnov, A., Yamasoe, M.A., Artaxo, P., 2003. High aerosol optical depth biomass burning events: A comparison of optical properties for different source regions. Geophys. Res. Lett. 30 (20), _eprint: https://onlinelibrary.wiley.com/doi/pdf/10.1029/2003GL017861.

Engelmann, R., Ansmann, A., Ohneiser, K., Griesche, H., Radenz, M., Hofer, J., Althausen, D., Dahlke, S., Maturilli, M., Veselovskii, I., Jimenez, C., Wiesen, R., Baars, H., Bühl, J., Gebauer, H., Haarig, M., Seifert, P., Wandinger, U., Macke, A., 2021. Wildfire smoke, Arctic haze, and aerosol effects on mixed-phase and cirrus clouds over the North Pole region during MOSAiC: an introduction. Atmos. Chem. Phys. 21 (17), 13397–13423, Publisher: Copernicus GmbH.

Evangeliou, N., Kylling, A., Eckhardt, S., Myroniuk, V., Stebel, K., Paugam, R., Zibtsev, S., Stohl, A., 2019. Open fires in Greenland in summer 2017: transport, deposition and radiative effects of BC, OC and BrC emissions. Atmos. Chem. Phys. 19 (2), 1393–1411.

Feltracco, M., Barbaro, E., Contini, D., Zangrando, R., Toscano, G., Battistel, D., Barbante, C., Gambaro, A., 2018. Photo-oxidation products of $\alpha$ -pinene in coarse, fine and ultrafine aerosol: A new high sensitive HPLC-MS/MS method. Atmos. Environ. 180, 149–155.

Feltracco, M., Barbaro, E., Spolaor, A., Vecchiato, M., Callegaro, A., Burgay, F., Vardè, M., Maffezzoli, N., Dallo, F., Scoto, F., Zangrando, R., Barbante, C., Gambaro, A., 2021. Year-round measurements of size-segregated low molecular weight organic acids in Arctic aerosol. Sci. Total Environ. 763, 142954.

Garrett, T., Brattstroem, S., Sharma, S., Worthy, D., Novelli, P., 2011. The role of scavenging in the seasonal transport of black carbon and sulfate to the Arctic. Geophys. Res. Lett. 38 (16).

Giardi, F., Becagli, S., Traversi, R., Frosini, D., Severi, M., Caiazzo, L., Ancillotti, C., Cappelletti, D., Moroni, B., Grotti, M., Bazzano, A., Lupi, A., Mazzola, M., Vitale, V., Abollino, O., Ferrero, L., Bolzacchini, E., Viola, A., Udisti, R., 2016. Size distribution and ion composition of aerosol collected at Ny-Ålesund in the spring–summer field campaign 2013. Rend. Lincei 27 (1720–0776).

Gilardoni, S., Heslin-Rees, D., Mazzola, M., Vitale, V., Sprenger, M., Krejci, R., 2023. Drivers controlling black carbon temporal variability in the Arctic lower troposphere. EGUsphere 2023, 1–31.

Gillett, N.P., Weaver, A.J., Zwiers, F.W., Flannigan, M.D., 2004. Detecting the effect of climate change on Canadian forest fires. Geophys. Res. Lett. 31 (18), _eprint: https://onlinelibrary.wiley.com/doi/pdf/10.1029/2004GL020876.

González, R., Toledano, C., Román, R., Fuertes, D., Berjón, A., Mateos, D., Guirado-Fuentes, C., Velasco-Merino, C., Antuña-Sánchez, J.C., Calle, A., Cachorro, V.E., de Frutos, Á.M., 2020. Daytime and nighttime aerosol optical depth implementation in CÆLIS. Geosci. Instrum. Methods Data Syst. 9, 417–433.

Huang, J., Jaeglé, L., 2017. Wintertime enhancements of sea salt aerosol in polar regions consistent with a sea ice source from blowing snow. Atmos. Chem. Phys. 17 (5), 3699–3712.

Iqbal, M., 1983. An Introduction to Solar Radiation. Academic Press.

Kasischke, E.S., Turetsky, M.R., 2006. Recent changes in the fire regime across the North American boreal region—Spatial and temporal patterns of burning across Canada and Alaska. Geophys. Res. Lett. 33 (9), _eprint: https://onlinelibrary.wiley.com/doi/pdf/10.1029/2006GL025677.

Kharuk, V.I., Ponomarev, E.I., 2017. Spatiotemporal characteristics of wildfire frequency and relative area burned in larch-dominated forests of Central Siberia. Russ. J. Ecol. 48 (6), 507–512.

Kyrö, E.-M., Kerminen, V.-M., Virkkula, A., Dal Maso, M., Parshintsev, J., Ruíz-Jimenez, J., Forsström, L., Manninen, H.E., Riekkola, M.-L., Heinonen, P., Kulmala, M., 2013. Antarctic new particle formation from continental biogenic precursors. Atmos. Chem. Phys. 13 (7), 3527–3546, Publisher: Copernicus GmbH.

Lynch, P., Reid, J., Westphal, D., Zhang, J., Hogan, T., Hyer, E., Curtis, C., Hegg, D., Shi, Y., Campbell, J., Rubin, J., Sessions, W., Turk, F., Walker, A., 2016. An 11-year global gridded aerosol optical thickness reanalysis (v1.0) for atmospheric and climate sciences. Geosci. Model Dev. 9 (4), 1489–1522.

Markowicz, K.M., Pakszys, P., Ritter, C., Zielinski, T., Udisti, R., Cappelletti, D., Mazzola, M., Shiobara, M., Xian, P., Zawadzka, O., Lisok, J., Petelski, T., Makuch, P., Karasiński, G., 2016. Impact of North American intense fires on aerosol optical properties measured over the European Arctic in July 2015. J. Geophys. Res.: Atmos. 121 (24), 14,487–14,512, _eprint: https://onlinelibrary.wiley.com/doi/pdf/10.1002/2016JD025310.

Mazzola, M., Viola, A.P., Lanconelli, C., Vitale, V., 2016. Atmospheric observations at the Amundsen-Nobile Climate Change Tower in Ny-Ålesund, Svalbard. Rend. Lincei 27 (1), 7–18.

McCarty, J.L., Smith, T.E.L., Turetsky, M.R., 2020. Arctic fires re-emerging. Nat. Geosci. 13 (10), 658–660, Number: 10 Publisher: Nature Publishing Group.

O'Dowd, C.D., Smith, M.H., Consterdine, I.E., Lowe, J.A., 1997. Marine aerosol, sea-salt, and the marine sulphur cycle: a short review. Atmos. Environ. 31 (1), 73–80.

Ohneiser, K., Ansmann, A., Chudnovsky, A., Engelmann, R., Ritter, C., Veselovskii, I., Baars, H., Gebauer, H., Griesche, H., Radenz, M., Hofer, J., Althausen, D., Dahlke, S., Maturilli, M., 2021. The unexpected smoke layer in the High Arctic winter stratosphere during MOSAiC 2019–2020. Atmos. Chem. Phys. 21 (20), 15783–15808, Publisher: Copernicus GmbH.

Paatero, P., Tapper, U., 1994. Positive matrix factorization: A non-negative factor model with optimal utilization of error estimates of data values. Environmetrics 5 (2), 111–126.

Pandolfi, M., Alados-Arboledas, L., Alastuey, A., Andrade, M., Angelov, C., Artiñano, B., Backman, J., Baltensperger, U., Bonasoni, P., Bukowiecki, N., Collaud Coen, M., Conil, S., Coz, E., Crenn, V., Dudoitis, V., Ealo, M., Eleftheriadis, K., Favez, O., Fetfatzis, P., Fiebig, M., Flentje, H., Ginot, P., Gysel, M., Henzing, B., Hoffer, A., Holubova Smejkalova, A., Kalapov, I., Kalivitis, N., Kouvarakis, G., Kristensson, A., Kulmala, M., Lihavainen, H., Lunder, C., Luoma, K., Lyamani, H., Marinoni, A., Mihalopoulos, N., Moerman, M., Nicolas, J., O'Dowd, C., Petäjä, T., Petit, J.-E., Pichon, J.M., Prokopciuk, N., Putaud, J.-P., Rodríguez, S., Sciare, J., Sellegri, K., Swietlicki, E., Titos, G., Tuch, T., Tunved, P., Ulevicius, V., Vaishya, A., Vana, M., Virkkula, A., Vratolis, S., Weingartner, E., Wiedensohler, A., Laj, P., 2018. A European aerosol phenomenology – 6: scattering properties of atmospheric aerosol particles from 28 ACTRIS sites. Atmos. Chem. Phys. 18 (11), 7877–7911, Publisher: Copernicus GmbH.

Quinn, P.K., Bates, T.S., Baum, E., Doubleday, N., Fiore, A.M., Flanner, M., Fridlind, A., Garrett, T.J., Koch, D., Menon, S., Shindell, D., Stohl, A., Warren, S.G., 2008. Short-lived pollutants in the Arctic: their climate impact and possible mitigation strategies. Atmos. Chem. Phys. 8 (6), 1723–1735, Publisher: Copernicus GmbH.

Román, R., González, R., Toledano, C., Barreto, Á., Pérez-Ramírez, D., Benavent-Oltra, J.A., Olmo, F.J., Cachorro, V.E., Alados-Arboledas, L., de Frutos, Á.M., 2020. Correction of a lunar-irradiance model for aerosol optical depth retrieval and comparison with a star photometer. Atmos. Meas. Tech. 13, 6293–6310.

Schmeisser, L., Backman, J., Ogren, J.A., Andrews, E., Asmi, E., Starkweather, S., Uttal, T., Fiebig, M., Sharma, S., Eleftheriadis, K., Vratolis, S., Bergin, M., Tunved, P., Jefferson, A., 2018. Seasonality of aerosol optical properties in the Arctic. Atmos. Chem. Phys. 18 (16), 11599–11622, Publisher: Copernicus GmbH.

Serreze, M.C., Barry, R.G., 2011. Processes and impacts of Arctic amplification: A research synthesis. Glob. Planet. Change 77 (1–2), 85–96.

Shaw, G.E., 1995. The Arctic haze phenomenon. Bull. Am. Meteorol. Soc. 76 (12), 2403–2413, Publisher: American Meteorological Society.

Sinyuk, A., Holben, B.N., Eck, T.F., Giles, D.M., Slutsker, I., Korkin, S., Schafer, J.S., Smirnov, A., Sorokin, M., Lyapustin, A., 2020. The AERONET Version 3 aerosol retrieval algorithm, associated uncertainties and comparisons to Version 2. Atmos. Meas. Tech. (6), 3375–3411.

Stockwell, C.E., Veres, P.R., Williams, J., Yokelson, R.J., 2015. Characterization of biomass burning emissions from cooking fires, peat, crop residue, and other fuels with high-resolution proton-transfer-reaction time-of-flight mass spectrometry. Atmos. Chem. Phys. 15 (2), 845–865, Publisher: Copernicus GmbH.

Stohl, A., 2006. Characteristics of atmospheric transport into the Arctic troposphere. J. Geophys. Res.: Atmos. 111 (D11), _eprint: https://onlinelibrary.wiley.com/doi/pdf/10.1029/2005JD006888.

Stohl, A., Klimont, Z., Eckhardt, S., Kupiainen, K., Shevchenko, V.P., Kopeikin, V.M., Novigatsky, A.N., 2013. Black carbon in the Arctic: the underestimated role of gas flaring and residential combustion emissions. Atmos. Chem. Phys. 13 (17), 8833–8855, Publisher: Copernicus GmbH.

Tomasi, C., Fuzzi, S., Kokhanovsky, A., 2017. Atmospheric Aerosols: Life Cycles and Effects on Air Quality and Climate. John Wiley & Sons, Google-Books-ID: 5bCGDQAAQBAJ.

Tomasi, C., Kokhanovsky, A.A., Lupi, A., Ritter, C., Smirnov, A., O'Neill, N.T., Stone, R.S., Holben, B.N., Nyeki, S., Wehrli, C., Stohl, A., Mazzola, M., Lanconelli, C., Vitale, V., Stebel, K., Aaltonen, V., de Leeuw, G., Rodriguez, E., Herber, A.B., Radionov, V.F., Zielinski, T., Petelski, T., Sakerin, S.M., Kabanov, D.M., Xue, Y., Mei, L., Istomina, L., Wagener, R., McArthur, B., Sobolewski, P.S., Kivi, R., Courcoux, Y., Larouche, P., Broccardo, S., Piketh, S.J., 2015. Aerosol remote sensing in polar regions. Earth-Sci. Rev. 140, 108–157.

Udisti, R., Bazzano, A., Becagli, S., Bolzacchini, E., Caiazzo, L., Cappelletti, D., Ferrero, L., Frosini, D., Giardi, F., Grotti, M., Lupi, A., Malandrino, M., Mazzola, M., Moroni, B., Severi, M., Traversi, R., Viola, A., Vitale, V., 2016. Sulfate source apportionment in the Ny-Ålesund (Svalbard Islands) Arctic aerosol. Rend. Lincei 27, 85–94.

Veraverbeke, S., Rogers, B.M., Goulden, M.L., Jandt, R.R., Miller, C.E., Wiggins, E.B., Randerson, J.T., 2017. Lightning as a major driver of recent large fire years in North American boreal forests. Nature Clim. Change 7 (7), 529–534, Number: 7 Publisher: Nature Publishing Group.

Virkkula, A., 2010. Correction of the calibration of the 3-wavelength Particle Soot Absorption Photometer (3$\lambda$ PSAP). Aerosol Sci. Technol. 44 (8), 706–712, Publisher: Taylor & Francis _eprint: https://doi.org/10.1080/02786826.2010.482110.

Voronova, O., Zima, A., Kladov, V., 2020. Anomalous wildfires in Siberia in Summer 2019. Atmos. Ocean. Phys. (56), 1042–1052.

Witek, M., Flatau, P., Teixeira, J., Westphal, D., 2007. Coupling an ocean wave model with a global aerosol transport model: A sea salt aerosol parameterization perspective. Geophys. Res. Lett. 34 (14).

Witze, A., 2020. The Arctic is burning like never before — and that's bad news for climate change. Nature 585 (7825), 336–337, Bandiera_abtest: a Cg_type: News Number: 7825 Publisher: Nature Publishing Group Subject_term: Forestry, Environmental sciences, Atmospheric science, Climate change.

Zangrando, R., Barbaro, E., Vecchiato, M., Kehrwald, N., Barbante, C., Gambaro, A., 2016. Levoglucosan and phenols in Antarctic marine, coastal and plateau aerosols. Sci. Total Environ. 544, 606–616.

Zielinski, T., Bolzacchini, E., Cataldi, M., Ferrero, L., Graßl, S., Hansen, G., Mateos, D., Mazzola, M., Neuber, R., Pakszys, P., Posyniak, M., Ritter, C., Severi, M., Sobolewski, P., Traversi, R., Velasco-Merino, C., 2020. Study of chemical and optical properties of biomass burning aerosols during long-range transport events toward the arctic in summer 2017. Atmosphere 11 (1), 84, Number: 1 Publisher: Multidisciplinary Digital Publishing Institute.